10-2003

A Mushy-Zone Rayleigh Number to Describe Interdendritic Convection During Directional Solidification of Hypoeutectic Pb-Sb and Pb-Sn Alloys

Surendra N. Tewari
Cleveland State University

R. Tiwari
Cleveland State University

A Mushy-Zone Rayleigh Number to Describe Interdendritic Convection during Directional Solidification of Hypoeutectic Pb-Sb and Pb-Sn Alloys

S.N. TEWARI and R. TIWARI

Based on measurements of the specific dendrite surface area (S_v), fraction of interdendritic liquid (ϕ), and primary dendrite spacing (λ_1) on transverse sections in a range of directionally solidified hypoeutectic Pb-Sb and Pb-Sn alloys that were grown at thermal gradients varying from 10 to 197 K cm^{-1} and growth speeds ranging from 2 to 157 μm s^{-1}, it is observed that $S_v = \lambda_1^{-1} S^{*-0.33}$ $(3.38 - 3.29\ \phi + 8.85\ \phi^2)$, where $S^* = D_l\ G_{\text{eff}}/V\ m_1\ C_o\ (k - 1)/k$, with D_l being the solutal diffusivity in the melt, G_{eff} being the effective thermal gradient, V being the growth speed, m_l being the liquidus slope, C_o being the solute content of the melt, and k being the solute partition coefficient. Use of this relationship in defining the mushy-zone permeability yields an analytical Rayleigh number that can be used to describe the extent of interdendritic convection during directional solidification. An increasing Rayleigh number shows a strong correlation with the experimentally observed reduction in the primary dendrite spacing as compared with those predicted theoretically in the absence of convection.

I. INTRODUCTION

NATURAL convection in the dendritic mushy zone is responsible for the nucleation of spurious grains[1] and the formation of channel segregates[2–9] in directionally solidified alloys. It produces radial[10,11,12] and longitudinal macrosegregations[13,14] and alters the cellular-dendritic and planar-cellular transitions.[15] It also appears to reduce the primary dendrite spacing.[13–18]

Numerical simulations of the transport phenomena during alloy solidification have shown some success in predicting some of the solidification defects in metal alloys,[19–22] but they have two serious limitations. First, the two-order-of-magnitude difference between the thermal and solutal length scales makes the three-dimensional computation very time consuming, and, second, the interdependence of the mushy-zone morphology, its permeability, and its convection does not allow an exact analysis of the problem. For example, the extent of convection depends upon the permeability of the mushy zone, but the convection alters the primary dendrite spacing and, hence, affects the permeability itself. Therefore, several attempts have been made to describe convection in terms of a nondimensional mushy-zone Rayleigh number.[4,7,23–26] The mushy-zone Rayleigh number proposed by Beckermann *et al.*[26] (R_{aB}) has been successful in describing the freckle initiation in nickel-based superalloy castings. However, the critical Rayleigh number for the onset of freckling has not been tested against the extensive freckling data available in the literature on other alloy systems, such as Pb-Sn,[3–7,9] Pb-Sb,[4] and Al-Mg.[8]

Describing convection through the mushy zone requires knowledge of the relationship between mushy-zone permeability (K) and its morphology, such as primary dendrite spacing (λ_1), fraction of interdendritic liquid (ϕ), *etc*. Many experimental[27–34] and numerical[35,36,37] investigations have been carried out to describe such a relationship. Experiments involving molten lead, to measure permeability in an Al-Cu alloy;[27] water, to determine permeability in a partially solidified Al-Si alloy;[28] and a transparent borneol-parafin system[29] showed that permeability is proportional to $(\phi)^n$, with n varying between 2 and 3.3. Others[31–34] used eutectic liquid to measure permeability in aluminum-copper alloys and observed it to follow the Kozeny–Carman relationship for flow through a porous bed:[38] $K = \phi^3/k_c S_v^2\ (1 - \phi)^2$, where S_v, the area of the solid-liquid interface per unit volume of the solid, is replaced by the dendrite surface area per unit volume, and k_c, a constant that depends upon the characteristic of the porous medium, was found to be about 5. Bhat *et al.*[37] analyzed the aforementioned experimental data and used numerical analysis to describe the permeability parallel to the primary dendrite array (K_y) and that perpendicular to the array (K_x) in the following manner:

$$K_Y = \begin{cases} 3.75 \times 10^{-4}\,\phi^2\lambda_1^{\,2} & \text{for } \phi < 0.65 \\ 2.05 \times 10^{-7}\,(\phi/1-\phi)^{10.739}\,\lambda_1^{\,2} & \text{for } 0.65 < \phi < 0.75 \\ 0.074\,(-\ln(1-\phi) - 1.49 + 2(1-\phi) - 0.5(1-\phi)^2)\,\lambda_1^{\,2} & \text{for } 0.75 < \phi < 1 \end{cases}$$

$$K_X = \begin{cases} 1.09 \times 10^{-3}\phi^{3.32}\,\lambda_1^{\,2} & \text{for } \phi < 0.65 \\ 4.04 \times 10^{-6}\,(\phi/1-\phi)^{6.7336}\,\lambda_1^{\,2} & \text{for } 0.65 < \phi < 0.75 \\ (-6.49 \times 10^{-2} + 5.43 \times 10^{-2}(\phi/1-\phi)^{0.25})\lambda_1^{\,2} & \text{for } 0.75 < \phi < 1 \end{cases}$$

Schneider *et al.*[20] used the experimental data reported by Bhat[32] to determine the following mushy-zone permeability: $K = 6 \times 10^{-4}\ \lambda_1^{\,2}\ \phi^3/(1-\phi)^2$. Beckermann *et al.*[26] have used this permeability relationship in describing their mushy-zone Rayleigh number. Yang *et al.*[24] have used $K = 3.75 \times 10^{-4}\ \phi^2\ \lambda_1^{\,2}$ to describe their nondimensional mushy-zone Rayleigh number.

S.N. TEWARI, Professor, and R. TIWARI, Graduate Student, are with the Chemical and Biomedical Engineering Department, Cleveland State University, Cleveland, OH 44115. Contact e-mail: s.tewari@csuohio.edu

Manuscript submitted February 4, 2003.

An examination of the previously described permeability relationships shows that they all assume permeability to depend only upon the primary dendrite spacing and fraction of interdendritic liquid. They do not take into account the role of side branching in determining the mushy-zone permeability. For example, one can visualize two dendrite arrays having equal λ_1 and ϕ values, but one array growing at a smaller gradient of constitutional supercooling (just beyond the cell-dendrite transition, having less-developed side branches) and the other growing at a larger gradient of constitutional supercooling (well-developed side branches). It is obvious that the permeability of the second array would be smaller than the first array, even though their λ_1 and ϕ values are identical.

The purpose of this study is to identify a mushy-zone Rayleigh number that accounts for the role of side branching. We will first carry out a detailed examination of the growth-parameter dependence of the specific dendrite surface area in directionally solidified Pb-Sb and Pb-Sn alloys, in order to obtain its dependence on the primary dendrite spacing, fraction of interdendritic liquid, and the parameter $S^* = D_l\, G_{\text{eff}}/(V\, m_l\, C_o\, (k-1)/k)$, where D_l is the solutal diffusivity in the melt, G_{eff} is the effective thermal gradient, V is the growth speed, m_l is the liquidus slope, C_o is the solute content of the melt, and k is the solute partition coefficient. The parameter S^* indicates the extent of side branching of dendrite arrays; it is equal to unity for a planar liquid-solid interface and decreases to zero with increasing side-branching tendency of dendrites. This value of S_v will be used to define a new mushy-zone Rayleigh number (R_{aM}) in a manner identical to that used by Beckermann *et al*.[26]

An appropriately defined mushy-zone Rayleigh number must be able to describe three important experimental observations. It should be able to correlate the extent of natural convection with the reduction in primary dendrite spacing; it should be able to relate the intensity of mushy-zone convection during directional solidification and the resulting longitudinal macrosegregation; and it should be useful in predicting the onset of channel-segregate formation. In this article, we will examine the first effect: primary-dendrite-spacing reduction due to mushy-zone convection. In a subsequent article, we will show that the Rayleigh number R_{aM} can also be used to predict the extent of longitudinal macrosegregation and onset of channel-segregate formation in a range of alloys.

II. EXPERIMENTAL

This study is mostly based on our earlier-reported and ongoing research on directionally solidified hypoeutectic Pb-Sb and Pb-Sn alloys. These samples were directionally solidified in flowing argon atmosphere, mostly in 0.7-cm-i.d. quartz ampoules, in a furnace arrangement where the furnace was translated and the sample was kept stationary to avoid the mechanical vibrations. Most of the samples were quenched after 9 to 10 cm of directional solidification (initial melt-column length at the onset of directional solidification was 18 to 20 cm) by a blast of helium gas circulating through a liquid nitrogen tank. Some samples were quenched by spraying water on the ampoule surface. A steady-state thermal gradient was maintained during the entire directional solidification process.[9] A range of alloy compositions (Pb-2.2 and 5.8 wt pct Sb, Pb-10 to 54.7 wt pct Sn) were directionally solidified at several thermal gradients (ranging from 10 to 197 K cm^{-1}) and growth speeds (ranging from 2 to 157 μm s^{-1}). Transverse sections through the mushy zone as a function of distance from the quenched array tips were utilized for measuring S_v; S_v is the ratio of the perimeter of the dendrite and its cross-sectional area. The sample-sectioning and image-analysis techniques have been described earlier.[39] The transverse images were also used to measure the corresponding fraction of interdendritic liquid. The primary-dendrite-spacing data used in this article correspond to $\sqrt{(A/N - 1)}$, where N is the number of dendrites on a sample cross-sectional area of A.

III. RESULTS AND DISCUSSION

A. *Experimental Characterization of the Mushy-Zone Morphology*

1. *Typical microstructures*

Figure 1 shows typical transverse mushy-zone microstructures as a function of distance from the quenched array tips in a Pb-5.8 wt pct Sb sample grown at 1.5 μm s^{-1} and 40 K cm^{-1}. The dendrites (light-colored features) in this sample are not well branched, because the growth condition is just beyond the cell-to-dendrite transition.

Figure 2 shows similar transverse sections through the quenched mushy zone of a Pb-23 wt pct Sn alloy sample that was directionally solidified at 2 μm s^{-1} with a thermal gradient of 52 K cm^{-1}. In this figure, the darker features are the lead dendrites, and the lighter features are the quenched interdendritic liquid. This sample has well-branched primary dendrites.

The typical microstructures shown in Figures 1 and 2 are from the as-milled sample surfaces without any subsequent polishing. The dendrite boundaries were traced from such micrographs for determining the area and the perimeter of the individual dendrites and the corresponding fraction of solid.

2. *Mushy-zone morphology*

Figure 3 shows a typical variation in the mean dendrite perimeter, mean dendrite area, and fraction of solid as a function of distance from the dendrite tip for a Pb-23 wt pct Sn alloy sample that was directionally solidified at 2 μm s^{-1} with a thermal gradient of 52 K cm^{-1}.

Data, such as those shown in Figure 3, were used to obtain the variation in S_v as a function of fraction of liquid (ϕ), shown in Figure 4. The scatter bars correspond to a ± 1 standard deviation. Figure 4(a) contains data from Pb-5.8 wt pct Sb alloys grown at 1, 1.5, and 3 μm s^{-1} at a thermal gradient of 140 K cm^{-1}. The 1 μm s^{-1} sample had a cellular morphology, the 1.5 μm s^{-1} sample was grown at the cell-to-dendrite transition, and the 3 μm s^{-1} sample had a dendritic morphology. Figure 4(b) contains data from Pb-5.8 wt pct Sb alloy samples grown at a thermal gradient of 40 K cm^{-1} at 3, 10, and 30 μm s^{-1}. All these three samples correspond to the well-branched primary dendrites. Figure 4(c) contains data from several Pb-Sn alloys

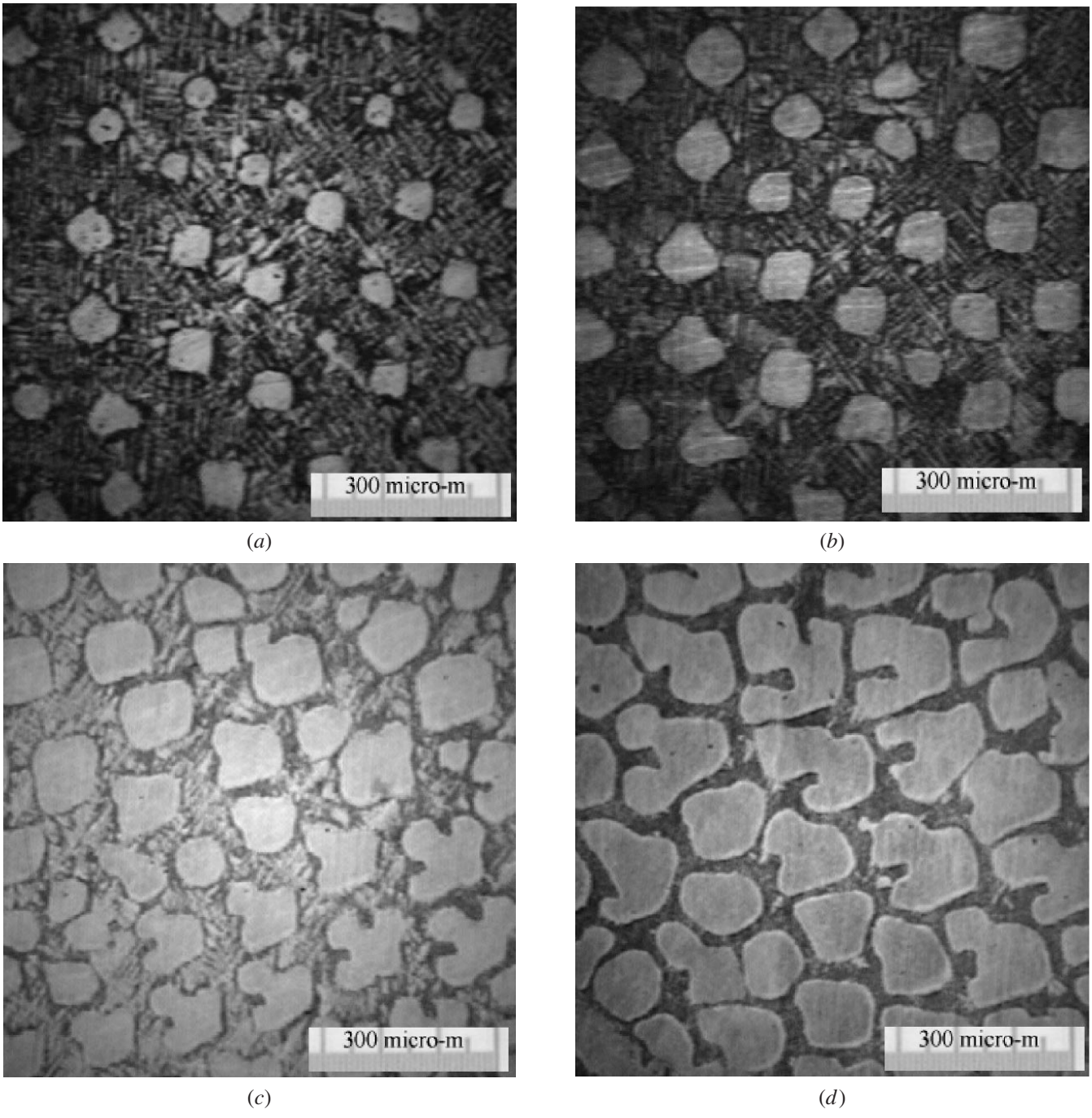

Fig. 1—Typical transverse microstructures of the mushy zone at varying distances from the quenched array tip in a directionally solidified Pb-5.8 wt pct Sb alloy grown at 1.5 μm s^{-1} with a thermal gradient of 40 K cm^{-1}: (*a*) 24 μm from the tip, (*b*) 71 μm from the tip, (*c*) 375 μm from the tip, and (*d*) 1065 μm from the tip.

grown with a well-branched dendrite morphology at varying thermal gradients and growth speeds. The scatter band is available for only the Pb-23 wt pct Sn sample grown at 2 μm s^{-1} with a thermal gradient of 53 K cm^{-1} and the Pb-30 wt pct Sn sample grown at 0.35 μm s^{-1} and 8 K cm^{-1}. It is not available for the other three Pb-Sn alloy samples that were examined some time ago. This figure shows that, generally, the dendrite specific surface area is low near the base of the mushy zone and increases toward the array tips. The side-branch coarsening, impingement, and coalescence that occur away from the array tips are responsible for this behavior.

B. *Mushy-Zone Permeability*

Let us compare the porous-bed permeability, defined by the Kozeny–Carman relationship $K = \phi^3/k_c\, S_v^2\, (1-\phi)^2$,[38] with the permeability relationships that have been used to define the mushy-zone Rayleigh numbers. Beckermann *et al.*[26] have used $K = 6 \times 10^{-4}\, \lambda_1^2\, \phi^3/(1-\phi)^2$, and Yang *et al.*[24]

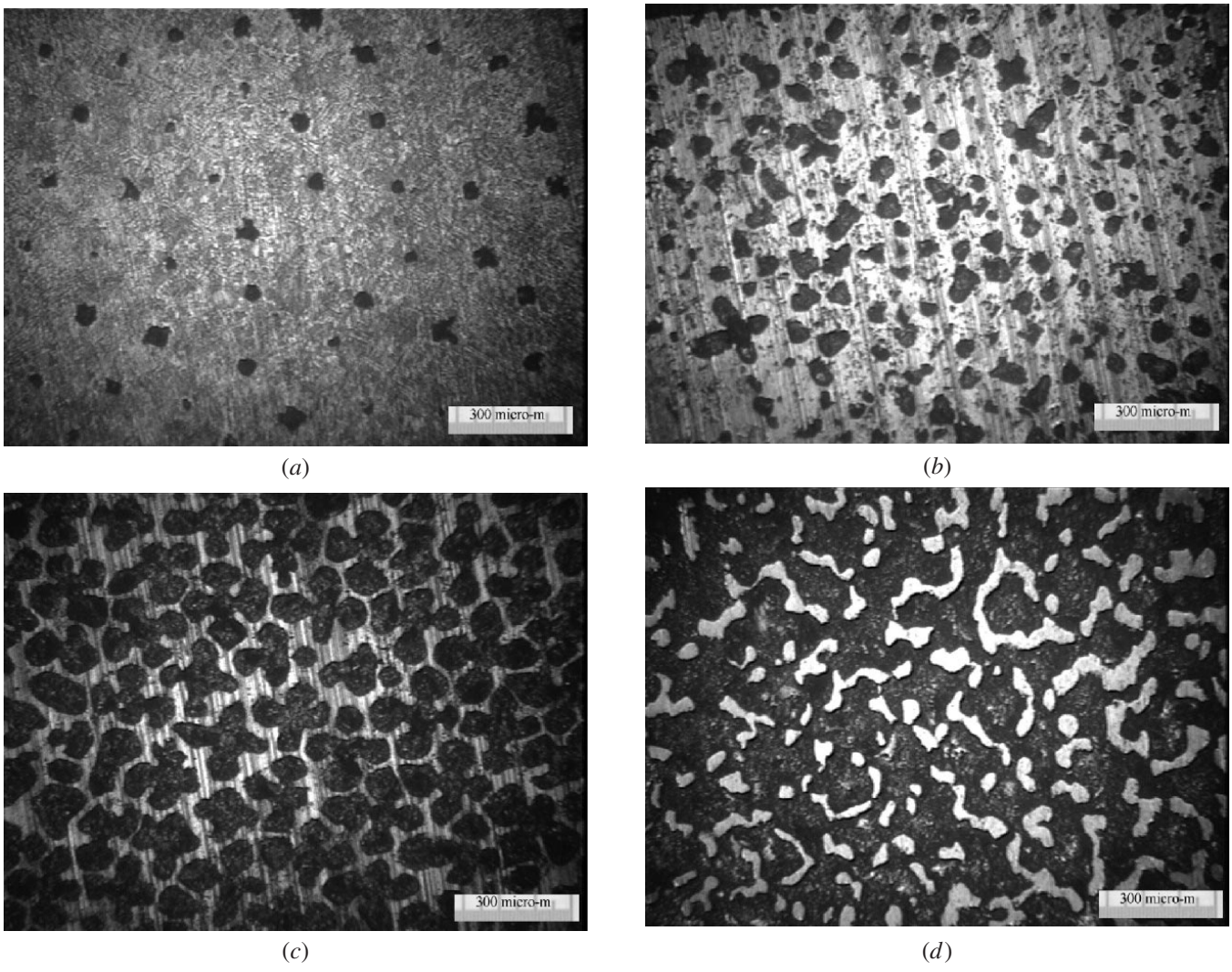

Fig. 2—Typical transverse microstructures of the mushy zone at varying distances from the quenched array tip in a directionally solidified Pb-23 wt pct Sn alloy grown at 2 μm s^{-1} with a thermal gradient of 52 K cm^{-1}: (*a*) 75 μm from the tip, (*b*) 222 μm from the tip, (*c*) 3562 μm from the tip, and (*d*) 17200 μm from the tip.

have used $K = 3.75 \times 10^{-4}\ \phi^2\ \lambda_1^2$. The first one would suggest that $S_v^2\ \lambda_1^2$ is constant and does not depend upon ϕ, and the second one would suggest that $S_v^2\ \lambda_1^2$ is proportional to $\phi/(1-\phi)^2$. However, as shown in Figure 5, which plots the parameter $S_v\ \lambda_1^2$ as a function of fraction of liquid for the Pb-Sb (Figure 5(a)) and Pb-Sn (Figure 5(b)) alloys, the experimental data do not support either of these deductions. The λ_1 values used here are those obtained experimentally from $\sqrt{(A/N - 1)}$, as indicated earlier in the experimental section. In the 20 to 90 pct fraction-of-liquid regime included in Figure 5, the parameter $S_v\ \lambda_1$ appears to have a linear dependence on the fraction of liquid; the solid lines represent the linear regressions. An examination of the various growth conditions represented in this figure shows that the samples with a higher side-branching tendency (higher growth speeds for a constant thermal gradient, or lower thermal gradients for a constant growth speed) tend to have higher slopes.

The slopes of the $S_v\ \lambda_1$ *vs* ϕ plots obtained from Figure 5 are plotted as a function of the parameter $S^* = D_l\ G_{\text{eff}}/(V\ m_l\ C_o(k-1)/k)$ on a log-log scale in Figure 6. Let us recall that S^* is very small for well-branched dendrites and increases toward unity as the side-branching tendency decreases. The physical properties[40–45] used for calculating S^* values are listed in Table I. The straight line represents the linear regression and the curved lines show the 95 pct confidence interval. The fit is not all that great: R^2 is only 0.44, but the tendency for the slope to decrease with the increasing S^* is evident. The slope of the linear-regression line in Figure 6 is 0.33. It suggests that instead of looking for a unique dependence between $S_v\ \lambda_1$ and the fraction of liquid in the mushy zone, as we have been doing so far, we should examine the possibility of such a relationship between $(S_v\ \lambda_1\ S^{*0.33})$ and the fraction of liquid.

Figure 7 plots $(S_v\ \lambda_1\ S^{*0.33})$ *vs* fraction of liquid for all the Pb-Sb and Pb-Sn alloy samples examined in this study. It represents 12 different directional solidification experiments and a total of 343 different mushy-zone cross sections. The best-fit polynomial to the data, indicated by the solid line, yields the following relationship:

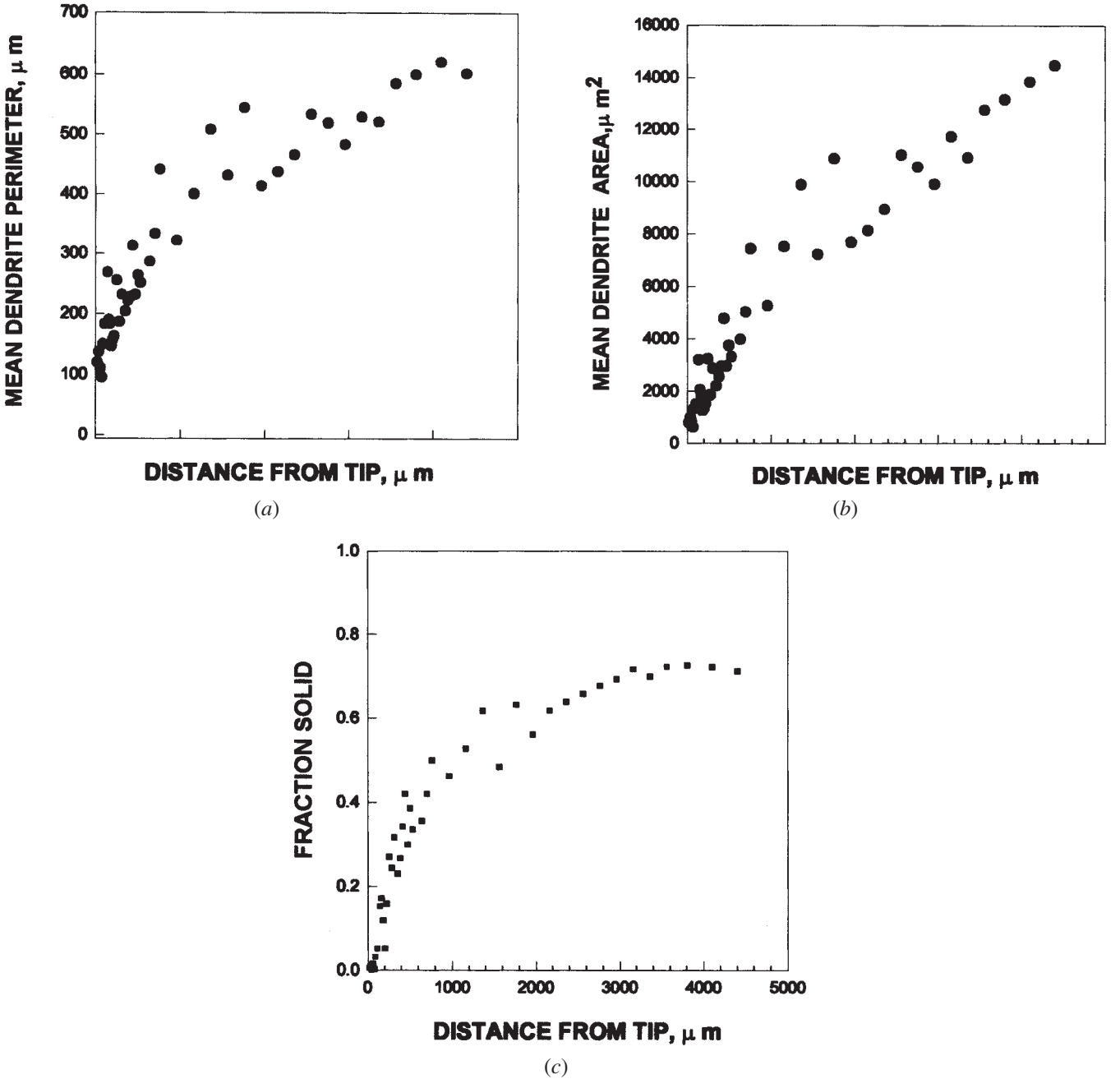

Fig. 3—Mushy-zone morphology in a Pb-23 wt pct Sn alloy directionally solidified at 2 μm s^{-1} with a thermal gradient of 52 K cm^{-1}: (*a*) mean dendrite perimeter *vs* distance from the array tip, (*b*) mean dendrite area *vs* distance from the array tip, and (*c*) fraction solid *vs* distance from the array tip.

$(S_v\ \lambda_1\ S^{*0.33}) = (3.38 \pm 0.33) - (3.29 \pm 1.29)\ \phi + (8.85 \pm 1.2)\ \phi^2$. Using this relationship to determine mushy-zone permeability, however, assumes that the dendrite morphology (perimeter and surface area) does not change during quenching. Thermal models of quenching may be developed to extract the dendrite morphology that existed during directional solidification from the quenched microstructures, but the analysis is expected to be quite complex and we have not made any attempt to do that. The extent of dendrite growth/coarsening during quenching would be expected to be dependent on the alloy composition and the growth conditions. We believe that this quenching artifact is the major source of scatter in Figure 7, which combines data from many experiments.

C. *Mushy-zone Rayleigh Number*

During directional solidification of hypoeutectic lead-antimony or lead-tin alloys, with melt on the top and solid below, the thermal profile in the mushy zone is stabilizing against natural convection. However, the solute content of the melt in the mushy zone increases as one moves from the array tips toward the eutectic isotherm at the mushy-zone bottom. Since the volumetric coefficient of expansion of the

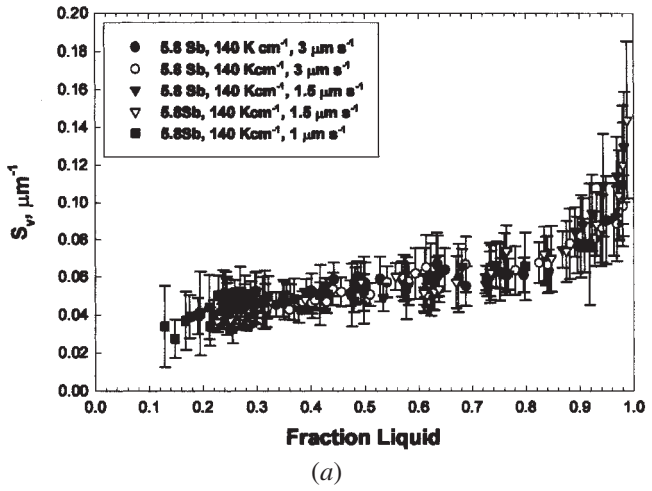

(*a*)

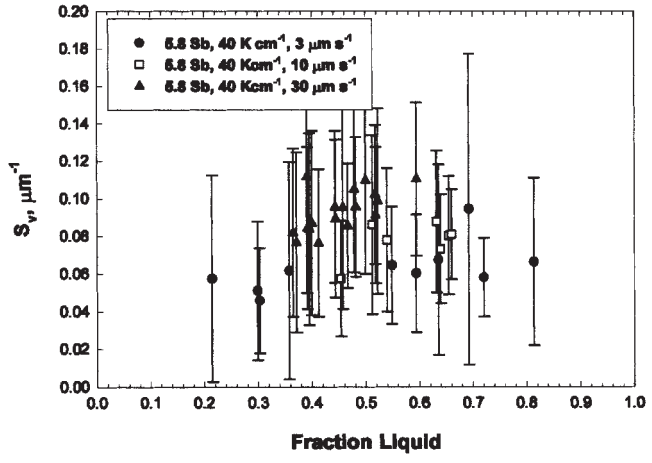

(*b*)

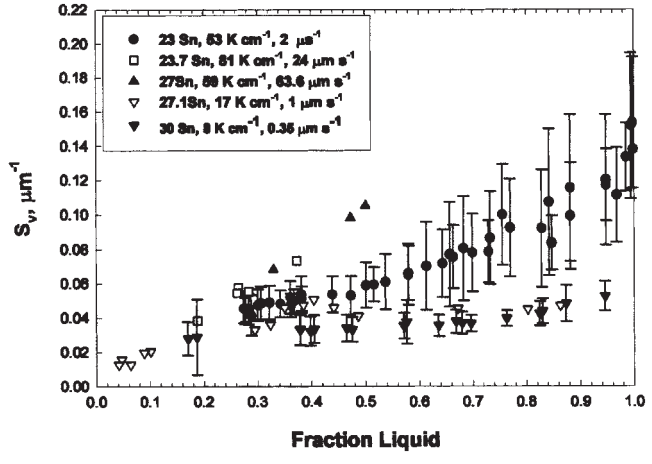

(*c*)

Fig. 4—Dependence of dendrite surface area per unit volume (S_v) on fraction liquid in the mushy zone. Error bars correspond to ±1 standard deviation: (*a*) Pb-5.8 wt pct Sb alloys grown at 140 K cm^{-1}, (*b*) Pb-5.8 wt pct Sb alloy grown at 40 K cm^{-1}, and (*c*) Pb-Sn alloys solidified at varying growth

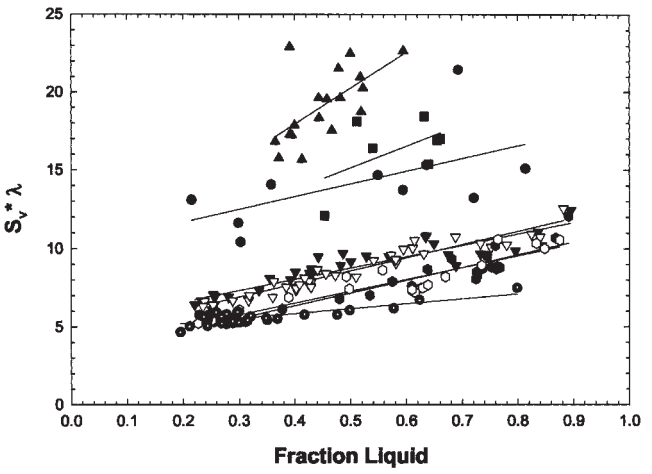

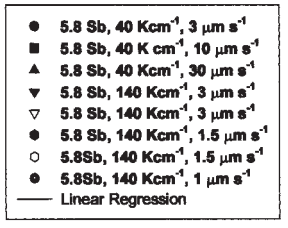

(*a*)

2D Graph 1

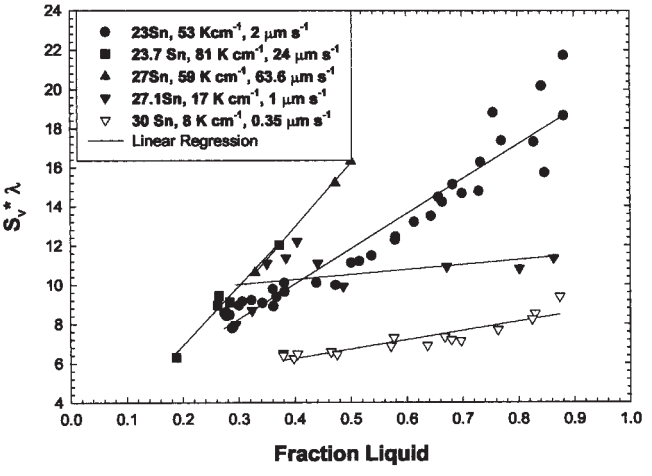

(*b*)

Fig. 5—Dependence of $S_v\lambda$ on the interdendritic fraction liquid (ϕ). The corresponding alloy composition, thermal gradient, and growth speeds are given in these figures. The solid lines denote the linear regression. Only the data from $\phi = 0.2$ to 0.9 are included in these figures: (*a*) Pb-5.8 wt pct Sb alloys and (*b*) Pb-Sn alloys.

melt due to the increasing solute content (β_c), for example, 5.83×10^{-3} (wt pct Sb)$^{-1}$ [40,41] is several orders of magnitude larger than its thermal coefficient of expansion (β_t), 1.22×10^{-4} K^{-1} [40,41] the solute contribution dominates and is responsible for the density inversion and convection in the mushy zone. Beckermann *et al.*[26] have defined a Rayleigh number, $R_{aB} = g(\Delta\rho/\rho_o)\ \kappa\, y/\alpha\, v$, to represent the extent of this mushy-zone convection. Here, g is the acceleration due to gravity, y is the distance from the array tip into the mushy zone, $\Delta\rho/\rho_o$ is the relative density inversion in the melt at y with respect to that at the tip, κ is the mean permeability averaged over the distance y, α is the melt thermal diffusivity, and v is the melt kinematic viscosity. They assume that the mean permeability is related to the mean solid fraction (ε_s): $\kappa = 6.10 \times 10^{-04}\ \lambda_1^2\ (1 - \varepsilon_s)^3/\varepsilon_s^2$, where λ_1 is the

primary dendrite spacing, and ε_s is the mean of the solid fraction from the tip to the distance, y. The mean solid fraction (ε_s) is obtained from the following relationship:

$$\varepsilon_s = y^{-1} \int_0^y \varepsilon_s(y)\, dy$$

where, using the Scheil equation, $\varepsilon_s(y)$ is assumed to be equal to $(1 - (1 - (y\ G_l/m_l\ C_o))^{(1/(k-1))})$. However, the assumption that permeability is equal to $6.10 \times 10^{-4}\ \lambda_1^2\ (1-\varepsilon_s)^3/\varepsilon_s^2$ is not supported by the experimental data, presented in Section III–B, because $S_v^2\ \lambda_1^2$ is not constant; it varies with S^* and ϕ. We will, therefore, incorporate the experimentally determined processing-parameter dependence of the dendrite specific surface area, $S_v = \lambda_1^{-1}\ S^{*-0.33}\ (3.38-3.29\ \phi + 8.85\ \phi^2)$, into the Kozeny–Carman permeability of a packed bed, $\kappa = \phi^3/4.2\ S_v^2\ (1-\phi)^2$,[38] in order to represent the permeability of a mushy zone during directional solidification. This permeability will then be used in the previously described relationship, $R_a = g\ (\Delta\rho/\rho_o)\ \kappa y/\alpha\nu$, to define the new mushy-zone Rayleigh number, R_{aM}.

Two opposing effects come into play as one moves away from the array tips into the mushy zone; the extent of the density inversion increases with the increasing distance, but the mush also becomes less permeable. It was suggested by Beckermann *et al.*[26] that the mushy-zone Rayleigh number increases as a function of distance from the array tips, it reaches a maximum at some depth, and then it begins to decrease again. However, in a recent publication, Frueh *et al.*[46] have shown that the maximum Rayleigh number is at the array tip and not in the mushy zone. They have argued that it is the convection in the destabilizing melt layer immediately ahead of the array tips that is the main source of "channel" nucleation, and not the convection deep within the mushy zone. The "channel segregates" form only if the solidification conditions permit the growth of these "channel nuclei" deeper into the mushy zone. Since the interdendritic convection is localized in the immediate vicinity of the array tips,[46,47] we decided to calculate the two Rayleigh numbers, R_{aB} and R_{aM}, at y equal to 30 times the corresponding dendrite-tip radius, to represent the extent of mushy-zone convection during directional solidification of Pb-Sb and Pb-Sn alloys. However, it should be pointed out that the observations described subsequently were also found to be valid when we used y equal to 50 times the radius to calculate R_{aB} and R_{aM}. We will use the tip radius and the primary-dendrite-spacing values predicted from the dendrite model due to Hunt and Lu[48] for determining R_{aB} and R_{aM}. This method does not require a prior knowledge of primary dendrite spacing to calculate the mushy-zone

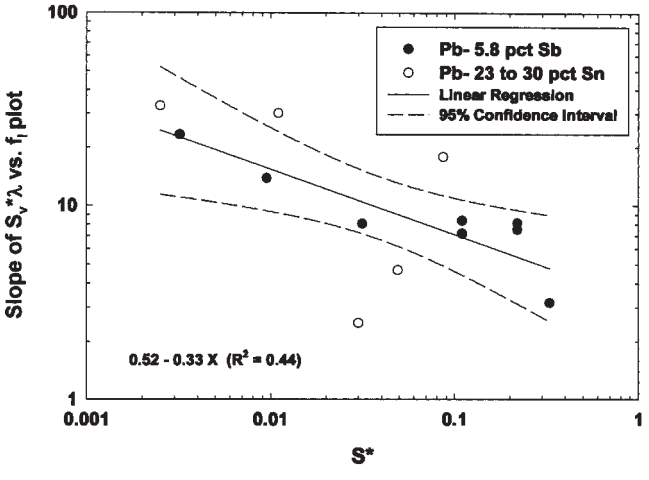

Fig. 6—Dependence of the slope of the $S_v\lambda$ versus ϕ plots on parameter S^*, where $S^* = D_l G_{eff}/[V m_l C_o(k-1)/k]$. Here, G_{eff} is the effective thermal gradient, V the growth speed, m_l the liquidus slope, C_o the alloy solute content, and k the solutal partition coefficient. The parameter S^* indicates the extent of side branching; it is equal to unity for plane front solidification and decreases to zero with increasing side-branching tendency of dendrites. The figure shows the linear regression and the corresponding 95 pct confidence interval.

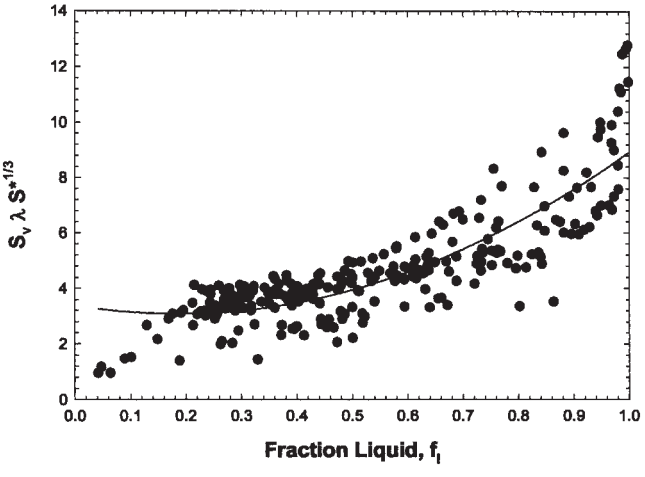

Fig. 7—Dependence of $S_v\lambda S^{*1/3}$ on the volume fraction interdendritic liquid, ϕ. The graph includes all the Pb-Sb and Pb-Sn alloys examined in this study, a total of 343 different mushy zone cross sections. The solid line represents the best polynomial fit through the experimental data: $S_v\lambda S^{*1/3} = (3.38 \pm 0.33) - (3.29 \pm 1.29)\ \phi + (8.85 \pm 1.2)\ \phi^2$.

Table I. Physical Properties of Pb-Sb and Pb-Sn Alloys

Physical Property	Pb-Sb	Reference	Pb-Sn	Reference
Thermal volumetric expansion coefficient (β_T), K^{-1}	1.22×10^{-4}	40, 41	1.15×10^{-4}	4
Solutal volumetric expansion coefficients (β_c), wt pct^{-1}	5.83×10^{-3}	40, 41	5.20×10^{-3}	4
Thermal diffusivity (α), $m^2\ s^{-1}$	1.70×10^{-5}	41, 45	1.10×10^{-5}	4
Kinemetic viscosity (ν), $m^2\ s^{-1}$	2.50×10^{-7}	42	2.47×10^{-7}	4
Solute diffusivity in melt (D_l), $cm^2\ s^{-1}$	3.00×10^{-5}	43	3.00×10^{-5}	4
Capillarity (Γ), m K	9.89×10^{-8}	40, 44, 45	assumed same as Pb-Sb	—
Thermal conductivity (solid)	$2.97 \times 10^{+1}$	41	assumed same as Pb-Sb	—
Thermal conductivity (liquid)	$1.54 \times 10^{+1}$	41	assumed same as Pb-Sb	—
Heat of fusion, $J\ m^{-3}$	$2.79 \times 10^{+8}$	45	assumed same as Pb-Sb	—

Rayleigh number. Following the procedure described by Beckermann *et al.*,[26] we also use the following relationships for calculating R_{aM}.

1. $(\Delta\rho/\rho_o) = \beta_T(T_y - T_t) + (C_y - C_t)$, where β_T and β_C are the thermal and solutal volumetric coefficients of expansion for the melt, respectively; T_t and C_t are the temperature of the melt and its solute content at the dendrite tip (as calculated from the Hunt–Lu[48] model), respectively; and T_y and C_y are the temperature and solute content at the distance y, respectively.
2. The assumption of a constant mushy-zone thermal gradient and local liquid-solid equilibrium: $C_y = C_t + y\ G_{\text{eff}}/m_l$.
3. A Scheil relationship to describe the fraction of liquid: $\phi_y = (C_y/C_t)^{(1/(k-1))}$.

D. *Mushy-Zone Convection and Reduction in Primary Dendrite Spacing*

Table II lists C_o, G_l, V, and $\lambda_{1(\text{experiment})}$ data for all the directionally solidified Pb-Sb and Pb-Sn alloy samples to be examined in the following analysis, together with the corresponding G_{eff}, and S^* values. It includes the theoretically predicted (Hunt–Lu model[48]) primary-spacing ($\lambda_{1\ \text{Theory}}$) values, and the corresponding R_{aB} and R_{aM} values for all the samples grown with a dendritic-array morphology. In the following discussion, we will also include other literature-reported data on directionally solidified Pb-Sb and Pb-Sn alloys.[13,49–52] However, we will consider only the dendritic-morphology samples and exclude those with a cellular morphology. All the data, except for those from Sarazin and Hellawell,[4,49] are for the steady-state directional solidification experiments, where either the cylindrical sample or the furnace setup was translated at a constant speed and constant thermal gradient to achieve directional solidification. The Sarazin and Hellawell[4,49] data are from the end-quench type directional solidification experiments, where the melt was poured into a ceramic mold, heated from the top and cooled from the bottom, and directional solidification was achieved by slow controlled cooling of the furnace. Since the thermal gradients and growth speeds did not remain constant during solidification of these samples, we have used their reported average values.

Let us first examine only those experiments where the alloy composition was kept constant and the growth speed was varied for several constant G_l values. Figure 8 plots the ratio of the experimentally observed and the theoretically predicted primary dendrite spacing as a function of R_{aB}, the mushy-zone Rayleigh number defined by Beckermann *et al.*,[26] for several Pb-Sb alloys. Figure 8(a) contains data for the Pb-5.8 wt pct Sb alloy generated during this research and also data marked as "JD" from Spittel and Lloyed[50] for similar alloy compositions (Pb-5.7 and Pb-5.2 wt pct Sb). This figure shows that an increasing mushy-zone convection, as indicated by an increasing R_{aB}, results in greater reduction in the primary dendrite spacing as compared with those predicted theoretically in the absence of convection. However, it is interesting to note that the data become segregated along various lines that represent constant thermal gradients. As the thermal gradient decreases from 197 to 20 K cm^{-1}, the linear-regression lines through the data shift to the right-hand side. A similar reduction in the primary dendrite spacing due to the mushy-zone convection requires a significantly higher R_{aB} for the samples grown at a lower thermal gradient than that grown at a higher thermal gradient. The same observations are also valid for the Pb-2.2 wt pct Sb alloy samples grown at various thermal gradients (Figure 8(b)).

Figure 9 combines all the available primary-dendrite-ratio data on the Pb-Sb alloys, including those listed as mixed (not a constant G_l, but a combination of G_l and V), and plots them together as a function of R_{aB}. The data marked as JD are from Reference 50. In this plot, the data from the high-antimony-content alloy, Pb-5.2 to 5.8 wt pct Sb (filled symbols), and those from the low-antimony-content alloy, Pb-2.2 wt pct Sb (open symbols), become segregated in two different regions. A similar reduction in the primary dendrite spacing due to the mushy-zone convection corresponds to a significantly higher R_{aB} for the high-antimony alloy than that for the low-antimony alloy.

Figure 10 plots the same primary-dendrite-ratio data (shown in Figure 9) as a function R_{aM}, the mushy-zone Rayleigh number defined in this article that includes the side-branching contribution in defining the mushy-zone permeability. Figure 10 also includes the Pb-Sb (mixed) data from Reference 50, marked as JD, and from Reference 49, marked as "Sarazin," for directionally solidified samples where the antimony content varied from 0.53 to 8.37 wt pct. Now the spacing-ratio data come together, irrespective of the thermal gradient or the antimony content, and show a definite linear trend of decrease in the primary-dendrite-spacing ratio as a function of increasing mushy-zone Rayleigh number. This suggests that including the side-branch contribution into the mushy-zone permeability relationship allows us to define a more consistent Rayleigh number.

Figure 11 combines all of our Pb-Sb and Pb-Sn alloy primary-spacing data with those available in the literature and plots them as a function of the two Rayleigh numbers, R_{aB} (Figure 11(a)) and R_{aM} (Figure 11(b)). The symbol "SH" indicates data from Reference 4, JD indicates data from reference 50, and "KVT" indicates data from Reference 51. This figure includes data from 164 different directional solidification experiments (80 for Pb-Sn alloys and 84 for Pb-Sb alloys). Figure 11(a) shows that the primary-dendrite-spacing ratios for the Pb-Sb and the Pb-Sn alloys become segregated into two different regimes. A similar decrease in the primary dendrite spacing due to the mushy-zone convection corresponds to an order-of-magnitude higher R_{aB} for the Pb-Sb alloys as compared with the Pb-Sn alloys. However, when the same primary-dendrite-spacing ratios are plotted as a function of R_{aM} (Figure 11(b)), not only is the scatter decreased, but, also, the data from the two alloys are pulled together into a single straight line. Figure 11(b) shows a very clear trend of primary-dendrite-spacing decease due to an increasing mushy-zone convection.

However, at this stage, the exact mechanism by which the mushy-zone convection brings about the decrease in the primary dendrite spacing is not clear. It may affect the dendrite-tip radius and, hence, alter the primary dendrite spacing; in this case, one would expect the spacing decrease to be accompanied by an increase in the tip radius. It is also possible that convection simply melts the side branches, especially near the

Table II. Growth Parameters and Rayleigh Numbers for Directionally Solidified Pb-Sb and Pb-Sn Alloys

Sample	C_o (wt pct)	G_l (K cm^{-1})	V μm s^{-1}	$\lambda_{1\ exptal}$ μm	G_{eff} (K cm^{-1})	S^*	$\lambda_{1\ Theory}$ (μm)	R_{aB}	R_{aM}
Ding (6Sb4)	Pb-5.8 Sb	140	2	200	95.6	0.1647	590.3	0.1046	0.37493
Ding (6Sb9)	Pb-5.8 Sb	140	3	163	95.6	0.1098	527.4	0.08453	0.1868
Ding (6Sb8)	Pb-5.8 Sb	140	3.5	176	95.6	0.0941	502.8	0.07708	0.14386
Ding (6Sb6)	Pb-5.8 Sb	140	4	193	95.6	0.0824	481.5	0.0709	0.11505
Ding (6Sb5)	Pb-5.8 Sb	140	8	173	95.6	0.0412	378.3	0.04427	0.03720
Ding (6Sb3)	Pb-5.8 Sb	140	10	170	95.6	0.033	348.6	0.0377	0.02619
Ding (6Sb2b)	Pb-5.8 Sb	140	20	158	95.6	0.0165	268.4	0.0225	0.00903
Yushi	Pb-5.8 Sb	120	10	166	81.9	0.0283	369.4	0.04957	0.02987
Yushi	Pb-5.8 Sb	120	30	153	81.9	0.0095	243.4	0.02171	0.00578
Kunal	Pb-5.8 Sb	82	2.5	202	56	0.0772	696.0	0.2552	0.37149
Kunal	Pb-5.8 Sb	82	30	199	56	0.0065	282.0	0.04276	0.00852
Ding/Neck	Pb-5.8 Sb	155	10	142	105.8	0.0365	335.6	0.03147	0.02397
Hui	Pb-5.8 Sb	40	3	227.1	27.3	0.0314	873.1	0.8364	0.51997
Hui	Pb-5.8 Sb	40	10	209.9	27.3	0.0095	565.8	0.3532	0.08929
Hui	Pb-5.8 Sb	40	30	205.1	27.3	0.0032	376.8	0.1571	0.01897
Hui	Pb-5.8 Sb	40	70	168.9	27.3	0.0014	274.7	0.08366	0.00594
Hui	Pb-5.8 Sb	40	157	121.1	27.3	7.0000	203.4	0.04588	0.00212
Dave/DrG	Pb-5.8 Sb	10	80	213	6.8	3.0000	488.8	1.067	0.02678
Dave/DrG	Pb-5.8 Sb	20	20	265	13.6	0.0024	587.1	0.76405	0.07443
Dave/DrG	Pb-5.8 Sb	20	50	197	13.6	9.5000	420.8	0.3929	0.02108
Dave/DrG	Pb-5.8 Sb	20	80	195	13.6	6.0000	354.7	0.2791	0.01123
Dave/DrG	Pb-5.8 Sb	40	20	199	27.3	0.0048	438.0	0.2121	0.03356
Wu	Pb-5.8 Sb	40	5	219	27.3	0.0189	728.1	0.5834	0.24339
Weng	Pb-2.2 Sb	164	4	109.8	112	0.2543	388.2	0.00489	0.04666
Weng	Pb-2.2 Sb	164	5	124.8	112	0.2035	369.7	0.00454	0.03091
Sb(4)	Pb-2.2 Sb	140	4	142	95.6	0.2171	420.3	0.00690	0.04990
Sb(6)	Pb-2.2 Sb	140	10	149	95.6	0.0869	316.0	0.00415	0.00930
Sb(7a)	Pb-2.2 Sb	140	15	136	95.6	0.0579	271.0	0.00310	0.00454
Sb(8a)	Pb-2.2 Sb	140	20	126	95.6	0.0435	241.7	0.00249	0.00276
Sb(9)	Pb-2.2 Sb	140	30	125	95.6	0.029	204.7	0.00181	0.0014
Ding	Pb-2.2 Sb	86	2.1	217	58.7	0.2539	612.2	0.02429	0.19880
Ding	Pb-2.2 Sb	86	2.5	223	58.7	0.2133	591.4	0.02298	0.14618
Ding	Pb-2.2 Sb	86	2.5	204	58.7	0.2133	591.4	0.02298	0.01461
Ding	Pb-2.2 Sb	86	3	201	58.7	0.1777	565.7	0.02129	0.10481
Ding	Pb-2.2 Sb	86	6	199	58.7	0.0889	454.9	0.01425	0.03013
Ding	Pb-2.2 Sb	86	10	180	58.7	0.0533	376.6	0.00995	0.01248
Ding	Pb-2.2 Sb	86	14	184	58.7	0.0381	330.3	0.00772	0.00709
Ding	Pb-2.2 Sb	86	18.2	171	58.7	0.0293	297.4	0.0063	0.00461
Ding	Pb-2.2 Sb	86	30	165	58.7	0.0178	242.6	0.00421	0.00207
Ding	Pb-2.2 Sb	40	1.25	203	27.3	0.1985	999.3	0.1467	0.74141
Ding	Pb-2.2 Sb	40	3	264	27.3	0.0827	773	0.09067	0.1607
Ding	Pb-2.2 Sb	40	5	239	27.3	0.0497	644.1	0.06373	0.06839
Ding	Pb-2.2 Sb	40	7	220	27.3	0.0355	567.6	0.04972	0.03795
Ding	Pb-2.2 Sb	40	10	212	27.3	0.0249	494.6	0.03803	0.02248
Hui	Pb-2.2 Sb	40	3	258.4	27.3	0.0827	773	0.09067	0.1608
Hui	Pb-2.2 Sb	40	10	235.4	27.3	0.0249	494.6	0.03803	0.02248
Hui	Pb-2.2 Sb	40	30	189.3	27.3	0.0083	319.6	0.01607	0.00420
Hui	Pb-2.2 Sb	40	70	133.1	27.3	0.0036	226.8	0.00813	0.00121
Hui	Pb-2.2 Sb	40	157	111.8	27.3	0.0016	163.4	0.00424	0.00038
RAJESH	Pb-10 Sn	110	3.5	125	75.1	0.207	537.9	0.00698	0.44389
RAJESH	Pb-10 Sn	110	4	134	75.1	0.1811	519.3	0.00587	0.35689
RAJESH	Pb-10 Sn	110	5	130	75.1	0.1449	485.9	0.00433	0.2469
RAJESH	Pb-10 Sn	110	6	130	75.1	0.1208	457.6	0.00333	0.1826
RAJESH	Pb-10 Sn	110	8	123	75.1	0.0906	413.1	0.00216	0.1133
SN001	Pb-10 Sn	110	10	116	75.1	0.0725	379.7	0.00152	0.07854
SN15	Pb-10 Sn	110	20	116	75.1	0.0363	287.3	0.00049	0.02548
(Ojha)DS3	Pb-23 Sn	52	10	150	35.5	0.0174	526.5	0.00736	0.43766
(Ojha)DS4	Pb-23 Sn	52	5	160	35.5	0.0347	683.9	0.02699	1.2268
(Ojha)DS5	Pb-23 Sn	52	2	188	35.5	0.0867	943.3	0.1543	4.9542
(Song, 18mm)L5	Pb-41.9 Sn	20	6	224	13.6	0.0048	1058.6	0.00969	7.35

Table II. Continued. Growth Parameters and Rayleigh Numbers for Directionally Solidified Pb-Sb and Pb-Sn Alloys

Sample	C_o (wt pct)	G_l (K cm^{-1})	V μm s^{-1}	$\lambda_{1\ exptal}$ μm	G_{eff} (K cm^{-1})	S^*	$\lambda_{1\ Theory}$ (μm)	R_{aB}	R_{aM}
(Song, 8mm)L6	Pb-32 Sn	60	8	159	40.9	0.0140	568	0.011	0.892
Rajesh 4a	Pb-33.4 Sn	75	8	166	51.2	0.0168	523.5	0.00975	0.75572
4b	Pb-38.7 Sn	75	8	137	51.2	0.0097	558.9	0.00701	1.075
4c	Pb-34 Sn	17	30	172	11.6	0.001	609.9	0.00068	0.6782
3g	Pb-27.1Sn	17	1	240	11.6	0.03	2014.6	0.2387	54.58
l	Pb-10 Sn	110	10	115	75.1	0.0725	379.7	0.00152	0.07825
lA	Pb-16.5 Sn	101	4	172	68.9	0.225	532.8	0.01724	1.84
5a	Pb-57.9 Sn	105	10	234	71.7	0.0066	498.0	0.00416	1.05971
5b	Pb-54.7 Sn	67	40	177	45.7	0.0012	365.6	0.00040	0.25595
3b	Pb-23.7 Sn	81	24	164	55.3	0.011	318.9	0.00165	0.08049
3c	Pb-23.4 Sn	77	6	185	52.6	0.0421	553.8	0.02271	0.66169
3d	Pb-27 Sn	59	64	155	40.3	0.0025	251.4	0.00023	0.03057
3f	Pb-30.3 Sn	20	6	208	13.7	0.0072	975.4	0.01207	4.072
3e	Pb-30.0 Sn	8	0.35	194	5.5	0.0495	3842	1.47	625.4

*In this table, C_o is solute content of the alloy, G_l is thermal gradient in the liquid at the dendrite tips, V is growth speed, $\lambda_{1\ exptl}$ is experimentally measured primary dendrite spacing, G_{eff} is effective thermal gradient, $\lambda_{1\ Theory}$ is primary spacing predicted from the Hunt–Lu model,[48] R_{aB} is Rayleigh number following the procedure presented by Beckerman *et al.*,[26] and R_{aM} is mushy-zone Rayleigh number, as defined in this article.

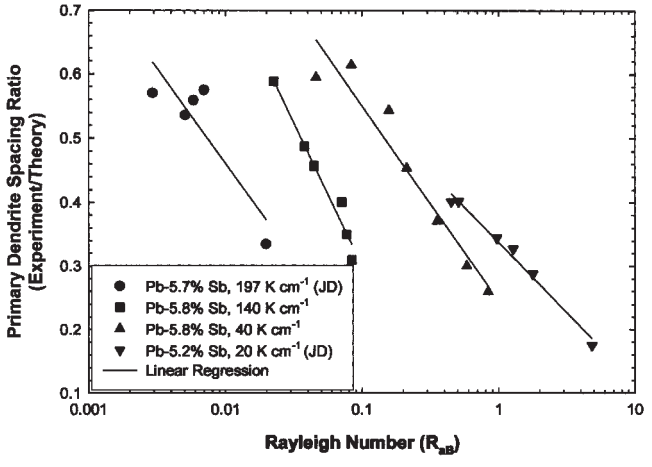

(*a*)

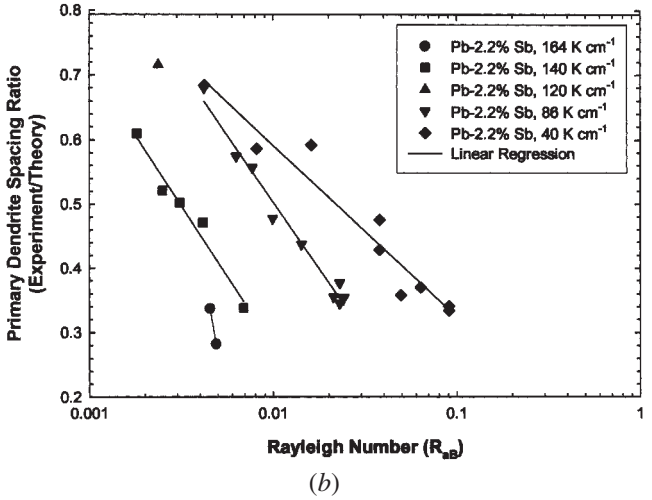

(*b*)

Fig. 8—Ratio of the experimentally observed and theoretically predicted primary dendrite spacings *vs* R_{aB}, the mushy-zone Rayleigh number defined by Beckermann *et al.*,[26] for Pb-Sb alloys directionally solidified at various growth speeds at several constant thermal gradients. The solid lines represent the corresponding linear regressions: (*a*) Pb-5.8, 5.7 and 5.2 wt pct Sb alloys (as indicated in Table I, the data identified as JD are from Ref. 49); and (*b*) Pb-2.2 wt pct Sb alloy.

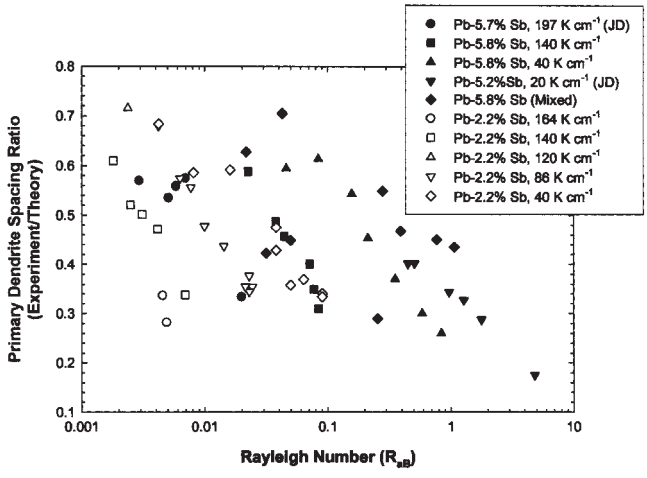

Fig. 9—A combined plot for the high antimony (Pb-5.2, 5.7, 5.8 wt pct Sb) and the low antimony (Pb-2.2 wt pct Sb) alloys that shows the ratio of the experimentally observed and theoretically predicted primary dendrite spacing *vs* R_{aB}.

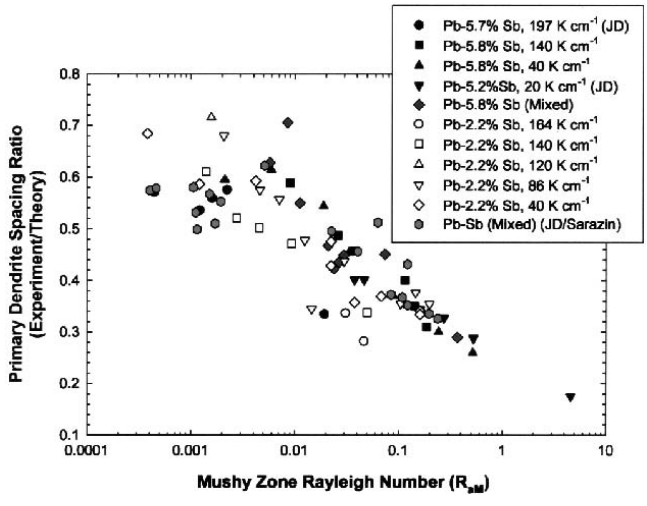

Fig. 10—Ratio of the experimentally observed and theoretically predicted primary dendrite spacing for all the Pb-Sb alloys examined in this study *vs* the mushy-zone Rayleigh number defined in this paper, R_{aM}.

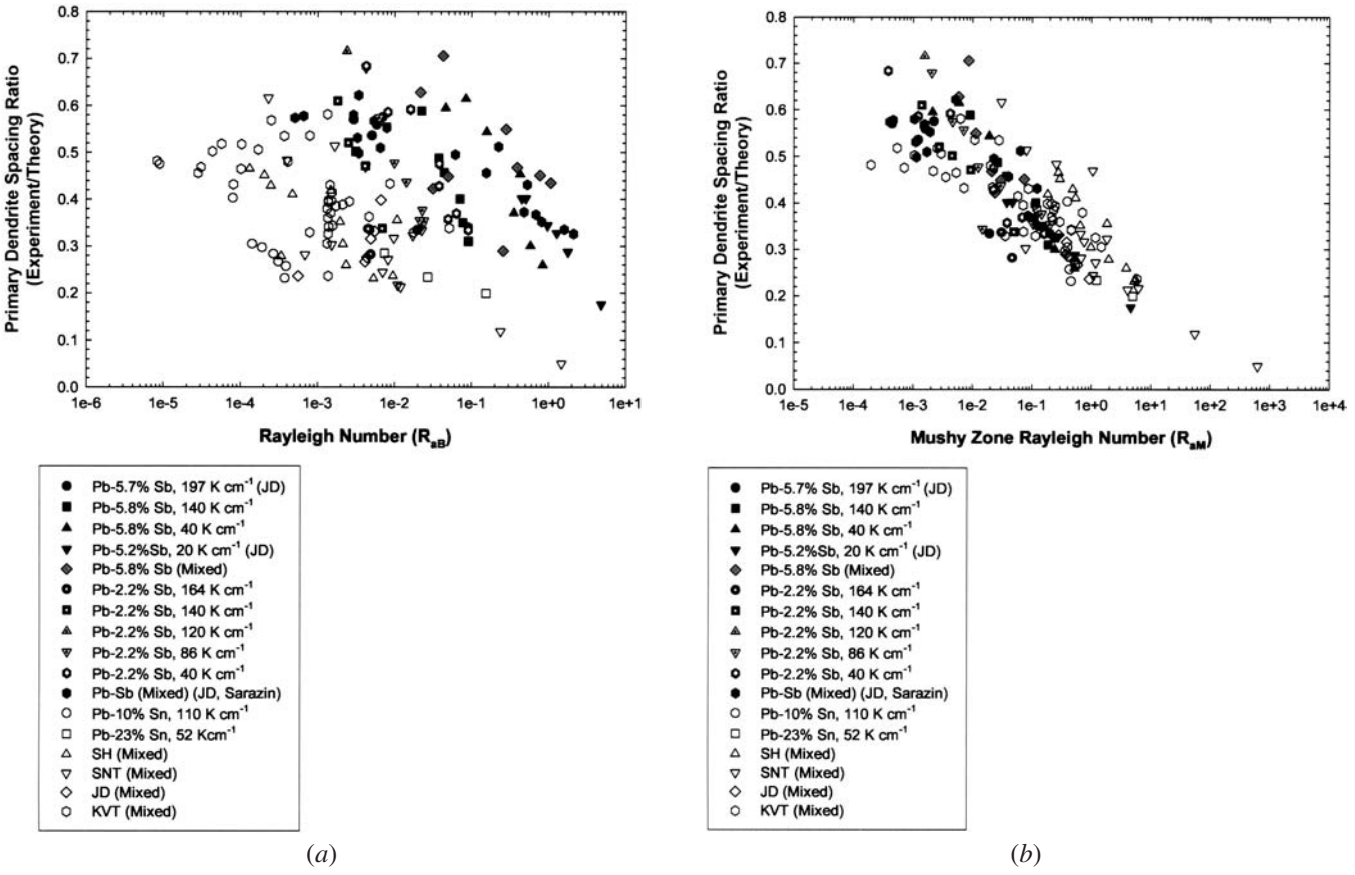

Fig. 11—A comparison of the two Rayleigh numbers, R_{aB} and R_{aM}. The filled symbols are for the Pb-Sb alloys and the open symbols are for the Pb-Sn alloys. As shown in Table I, the data represented as JD are from Ref. 50, those indicated as SH are from Ref. 4, those identified as KVT are from Ref. 51 and those indicated as SNT are from our own research: (*a*) Ratio of the experimentally observed and theoretically predicted primary dendrite spacing *vs* R_{aB}, and (*b*) ratio of the experimentally observed and theoretically predicted primary dendrite spacing *vs* R_{aM}.

array tips and, thus, allows the neighboring primary dendrites to come closer. The exact mechanism can only be identified by a quantitative comparison of the mushy-zone morphology between terrestrially grown samples and those grown in a near-absence of convection in the low-gravity environment of space.

IV. SUMMARY OF RESULTS

In this study, 343 different transverse sections in the mushy zone have been examined in directionally solidified hypoeutectic Pb-Sb and Pb-Sn alloys grown at varying thermal gradients and growth speeds, in order to determine the processing-parameter dependence of dendrite specific surface area, S_v. It is observed that $S_v = \lambda_1^{-1} S^{*-0.33} (3.38 - 3.29\ \phi + 8.85\ \phi^2)$, where λ_1 is the primary dendrite spacing and ϕ is the fraction of liquid in the mushy zone. The parameter S^* represents the extent of side branching and is given as $S^* = D_l G_{\text{eff}} / V\, m_l\, C_o\, (k-1)/k$, where D_l is the solutal diffusivity in the melt, G_{eff} is the effective thermal gradient, V is the growth speed, m_l is the liquidus slope, C_o is the solute content of the melt, and k is the solute partition coefficient.

Incorporation of the previous S_v relationship into the Kozney–Carman[38] relationship for a packed bed allows one to define a mushy-zone permeability that accounts for the extent of side-branch formation. When this permeability is incorporated into the approach taken by Beckermann *et al.*,[26] it allows us to define an analytical Rayleigh number, R_{aM}, that can be used to represent the extent of convection in the mushy-zone during directional solidification. The experimentally observed reduction in primary dendrite spacing due to convection shows a strong and consistent correlation with increasing R_{aM}. As will be shown in a subsequent publication, this mushy-zone Rayleigh number also shows an outstanding correlation with the experimentally observed longitudinal macrosegregation and can be used as a predictive tool for the onset of channel-segregate formation.

ACKNOWLEDGMENTS

This research was supported by the Microgravity Materials Science Research Program at the NASA–Marshall Space Flight Center (Huntsville, AL).

REFERENCES

1. T.M. Pollock and W.H. Murphy: *Metall. Mater. Trans. A*, 1996, vol. 27A, pp. 1081-94.
2. A.F. Giamei and B.H. Kear: *Metall. Trans.*, 1970, vol. 1, pp. 2185-92.
3. N. Streat and F. Weinburg: *Metall. Trans.*, 1972, vol. 3, pp. 3181-84.

4. J.R. Sarazin and A. Hellawell: *Metall. Trans. A*, 1988, vol. 12A, pp. 1861-71.
5. L. Wang, V. Laxmanan, and J.F. Wallace: *Metall. Trans. A*, 1988, vol. 19A, pp. 2687-94.
6. V. Laxmanan, A. Studer, L. Wang, J.F. Wallace, and E.A. Winsa: *NASA TM 89885*, NASA, Arlington, VA, 1986, pp. 1-35.
7. M.I. Bergman, D.R. Fearn, J. Bloxham, and M.C. Shannon: *Metall. Mater. Trans. A*, 1997, vol. 28A, pp. 859-66.
8. N. Mori and O. Keisaku: *Metall. Trans. A*, 1991, vol. 22A, pp. 1663-72.
9. S.N. Tewari and R. Shah: *Metall. Mater. Trans. A*, 1996, vol. 27A, pp. 1353-62.
10. M.H. Burden, D.J. Hebditch, and J.D. Hunt: *J. Cryst. Growth*, 1973, vol. 20, pp. 121-24.
11. J.D. Verhoeven, J.T. Mason, and R. Trivedi: *Metall. Trans. A*, 1996, vol. 17A, pp. 991-1000.
12. S.N. Tewari and M.A. Chopra: *Microgravity Sci. Technol*., 1990, vol. 3, pp. 99-106.
13. S.N. Tewari and R. Shah: *Metall. Trans. A*, 1991, vol. 23A, pp. 3383-92.
14. S.N. Ojha, G. Ding, Y. Lu, J. Reye, and S.N. Tewari: *Metall. Mater. Trans. A*, 1999, vol. 30A, pp. 2167-71.
15. R. Trivedi, H. Miyahara, P. Mazumder, E. Simsek, and S.N. Tewari: *J. Cryst. Growth*., 2000, vol. 222, pp. 365-79.
16. M.D. Dupouy, D. Camel, and J.J. Favier: *J. Cryst. Growth*, 1993, vol. 126, pp. 480-88.
17. M.D. Dupouy, D. Camel, and J.J. Favier: *Acta Metall*., 1989, vol. 37, pp. 1143-57.
18. H. Yu, K.N. Tandon, and J.R. Cahoon: *Metall. Mater. Trans. A*, 1997, vol. 28A, pp. 1245-50.
19. W.D. Bennon and F.P. Incropera: *Int. J. Heat Mass Transfer*, 1987, vol. 30, pp. 2161-70.
20. M.C. Schneider, J.P. Gu, C. Beckermann, W.J. Boettinger, and U.R. Kattner: *Metall. Mater. Trans. A*, 1997, vol. 28A, pp. 1517-31.
21. S.D. Felicelli, D.R. Poirier, and J.C. Heinrich: *Metall. Mater. Trans. A*, 1998, vol. 29A, pp. 847-55.
22. C. Frueh, D.R. Poirier, and S.D. Felicelli: *Mater. Sci. Eng. A*, 2002, vol. A 328, pp. 245-55.
23. S. Tait and C. Jaupart: *J. Geophys. Res*., 1992, vol. 97, pp. 6735-56.
24. W. Yang, W. Chen, K.M. Chang, S. Mannan, and J. deBarbadillo: *Metall. Mater. Trans. A*, 2001, vol. 32A, pp. 397-403.
25. H. Jun, R. Tiwari, X. Wu, S.N. Tewari, and R. Trivedi: *Metall. Mater. Trans. A*., 2002, vol. 33A, pp. 3499-510.
26. C. Beckermann, J.P. Gu, and W.J. Boettinger: *Metall. Mater. Trans. A*, 2000, vol. 31A, pp. 2545-52.
27. T.S. Piwonka and M.C. Flemings: *Trans. AIME*, 1966, vol. 236, pp. 1157-65.
28. D. Apelian, M.C. Flemings, and R. Mehrabian: *Metall. Trans*., 1974, vol. 5, pp. 2533-37.
29. K. Murakami and T. Okamoto: *Acta Metall*., 1984, vol. 32 (10), pp. 1741-44.
30. D.R. Poirier and S. Ganesan: *Mater. Sci. Eng. A*., 1993, vol. 171A, pp. 231-40.
31. D.R. Poirier and P. Ocansey: *Matls. Sci. Eng*., 1993, vol. A171, pp. 231-40.
32. M.C. Bhat: Ph.D. Thesis, The University of Arizona, Tucson, AR, 1995.
33. A.J. Duncan, Q. Han, and S. Viswanathan: *Metall. Mater. Trans. B*, 1999, vol. 30B, pp. 745-50.
34. ϕ. Nielson, L. Arnberg, A. Mo, and H. Thevick: *Metall. Mater. Trans. A*, 1999, vol. 30A, pp. 2455-62.
35. B. Goyeau, T. Benihaddadene, D. Gobin, and M. Quintard: *Metall. Mater. Trans. B*, 1999, vol. 30B, pp. 613-22.
36. D.R. Poirier: *Metall. Trans. B*, 1987, vol. 18B, pp. 245-55.
37. M.S. Bhat, D.R. Poirier, and J.C. Heinrich: *Metall. Mater. Trans. B*, 1995, vol. 26B, pp. 1049-56.
38. *Transport Phenomena in Metallurgy*, G.H. Geiger and D.R. Poirier, eds., Addision-Wesley Publishing Company, Reading, MA, 1973, p. 92.
39. L. Yu, G.L. Ding, J. Reye, S.N. Ojha, and S.N. Tewari: *Metall. Mater. Trans. A*, 2000, vol. 31A, pp. 2275-85.
40. E.T. Turkdogan: *Physical Chemistry of High Temperature Technology*, Academic Press, New York, NY, 1980, p. 89.
41. *Smithells Metals Reference Book*, 7th ed., E.A. Brandes and G.B. Brooks, eds., Buterworth-Heinemann Ltd., Oxford, United Kingdom., 1992, pp. 14-18 and 14-2.
42. E. Gebhardt and K. Kostlin: *Z. Metallkd*., 1957, vol. 48, pp. 636-40.
43. K. Niwa, M. Shimoji, S. Kado, Y. Watanabe, and T. Yokokawa: *Trans. AIME*, 1957, vol. 209, pp. 96-101.
44. M. Gunduz and J.D. Hunt: *Acta Mater*., 1985, vol. 33, pp. 1651-58.
45. R. Hultgren, R.L. Orr, P.D. Anderson, and K.K. Kelley: *Selected Values of Thermodynamic Properties of Metals and Alloys*, John Wiley & Sons, New York, NY, 1963, pp. 206, 247, and 893.
46. C. Frueh, D.R. Poirier, R.G. Erdmann, and S.D. Felicelli: *Mater. Sci. Eng. A*, 2003, vol. 345, pp. 72-80.
47. P.K. Sung, D.R. Poirier, and S.D. Felicelli: *Metall. Mater. Trans. A*, 2001, vol. 202, pp. 202-07.
48. J.D. Hunt and S.Z. Lu: *Metall. Mater. Trans. A*, 1996, vol. 27A, pp. 611-23.
49. J.R. Sarazin: Ph.D. Thesis, Michigan Technological University, Houghton, MI, 1990, pp. 1-190 (Table 4, p. 71).
50. J.A. Spittel and D.M. Lloyd: *Int. Conf. on Solidification and Casting*, 1977, vol. 1, pp. 15-20.
51. C.M. Klaren, J.D. Verhoeven, and R. Trivedi: *Metall. Trans. A*, 1980, vol. 11A, pp. 1853-61.
52. M.A. Chopra and S.N. Tewari: *Metall. Trans. A*, 1991, vol. 22A, pp. 2467-74.